

See discussions, stats, and author profiles for this publication at: <https://www.researchgate.net/publication/236641077>

High Thermoelectric Performance via Hierarchical Compositionally Alloyed Nanostructures

ARTICLE in JOURNAL OF THE AMERICAN CHEMICAL SOCIETY · MAY 2013

Impact Factor: 12.11 · DOI: 10.1021/ja403134b · Source: PubMed

CITATIONS

53

READS

122

13 AUTHORS, INCLUDING:



Lidong Zhao

Université Paris-Sud 11

94 PUBLICATIONS 2,197 CITATIONS

SEE PROFILE



Shiqiang Hao

Northwestern University

48 PUBLICATIONS 718 CITATIONS

SEE PROFILE



Chun-I Wu

Michigan State University

27 PUBLICATIONS 1,315 CITATIONS

SEE PROFILE



Kanishka Biswas

Jawaharlal Nehru Centre for Advanced Scienti...

80 PUBLICATIONS 2,368 CITATIONS

SEE PROFILE

High Thermoelectric Performance via Hierarchical Compositionally Alloyed Nanostructures

Li-Dong Zhao,[†] Shiqiang Hao,^{‡,⊥} Shih-Han Lo,^{‡,⊥} Chun-I Wu,[§] Xiaoyuan Zhou,^{||} Yeseul Lee,[†] Hao Li,[†] Kanishka Biswas,[†] Timothy P. Hogan,[§] Ctirad Uher,^{||} C. Wolverton,[‡] Vinayak P. Dravid,[‡] and Mercouri G. Kanatzidis^{*,†}

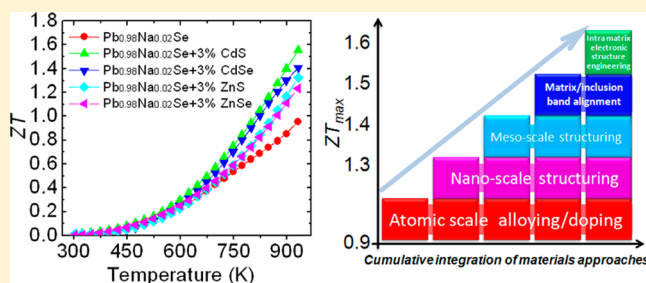
[†]Department of Chemistry and [‡]Department of Materials Science and Engineering, Northwestern University, Evanston, Illinois 60208, United States

[§]Department of Electrical and Computer Engineering, Michigan State University, East Lansing, Michigan 48824, United States

^{||}Department of Physics, University of Michigan, Ann Arbor, Michigan, 48109, United States

S Supporting Information

ABSTRACT: Previous efforts to enhance thermoelectric performance have primarily focused on reduction in lattice thermal conductivity caused by broad-based phonon scattering across multiple length scales. Herein, we demonstrate a design strategy which provides for simultaneous improvement of electrical and thermal properties of p-type PbSe and leads to $ZT \sim 1.6$ at 923 K, the highest ever reported for a tellurium-free chalcogenide. Our strategy goes beyond the recent ideas of reducing thermal conductivity by adding two key new theory-guided concepts in engineering, both electronic structure and band alignment across nanostructure–matrix interface. Utilizing density functional theory for calculations of valence band energy levels of nanoscale precipitates of CdS, CdSe, ZnS, and ZnSe, we infer favorable valence band alignments between PbSe and compositionally alloyed nanostructures of $\text{CdS}_{1-x}\text{Se}_x/\text{ZnS}_{1-x}\text{Se}_x$. Then by alloying Cd on the cation sublattice of PbSe, we tailor the electronic structure of its two valence bands (light hole L and heavy hole Σ) to move closer in energy, thereby enabling the enhancement of the Seebeck coefficients and the power factor.



INTRODUCTION

Thermoelectric generation technology, a type of solid-state 'heat engine' capable of converting heat to electricity, is expected to play an important role in energy generation. The key parameter that defines the efficiency of thermoelectric materials the 'thermoelectric figure of merit' ZT is derived from a combination of three properties: the thermal conductivity (κ), the electrical conductivity (σ), and the Seebeck coefficient (S) as well as the absolute temperature (T):^{1–5} $ZT = (S^2\sigma/\kappa)T$. The well-known interdependence of S , σ , and κ complicates efforts in developing strategies for improving a material's average ZT above 2.0, a feat that could revolutionize the field of thermal energy conversion especially using less expensive, more earth abundant materials. An effective strategy for improving ZT involves reducing the lattice thermal conductivity, particularly through introducing nanoscale precipitates in bulk matrix or compacting nanostructural grain-sized materials.^{6–11} In most of these cases, however, the power factor is also reduced relative to the single-phase parent material because the nanoprecipitates and corresponding interfaces increase carrier scattering. Approaches to enhance the power factor ($S^2\sigma$) include modifying the band structure by electronic resonance states,¹² designing quantum confinement effects,¹³ and electron

energy barrier filtering¹⁴ to generate enhanced Seebeck coefficients. Unfortunately, these efforts have not yet produced clear winning combinations exhibiting notable enhancements. Nearly barrierless carrier transport between the endotaxially aligned components can minimize deterioration of the hole mobility and electrical conductivity and retain the high power factor of a good thermoelectric material.^{15,16}

Remarkable progress has recently been made with exceptional ZT in both p- and n-type PbTe systems through nanostructuring,⁶ hierarchical architecting,⁷ and band structure engineering (resonant states¹² and convergence¹⁷). These advanced thermoelectric materials are based on Te which is scarce in its earth abundance and consequently quite costly. PbSe is now attracting increasing attention because of the 50-fold greater earth abundance of Se, which is also almost 5 times less expensive than Te. Although PbSe combines several attractive features such as higher melting point, lower cost, and higher operation temperatures,¹⁸ its electronic structure is not as advantageous as that of PbTe. Following a few studies performed several decades ago, PbSe was subsequently largely

Received: March 28, 2013

Published: May 6, 2013

neglected in favor of PbTe, because of the more desirable band structure of the latter for thermoelectricity. Recent work, however, has shown that ZT s as high as ~ 1.2 can be obtained at ~ 900 K for n-type PbSe^{9,19} and ~ 1.2 at ~ 850 K for p-type PbSe.²⁰ Theoretical calculations suggest that p-type PbSe can potentially reach a ZT of ~ 1.8 at 923 K,²¹ indicating tantalizing prospects for further improvements in ZT values in this system.

The electronic band structure of PbSe is not as favorable as that of PbTe because the two key valence bands (light hole L and heavy hole Σ) are energetically much farther apart in PbSe. The L – Σ band separation in PbTe is 0.15 eV compared to 0.26 eV in PbSe.²² Thus as the temperature increases, in the case of PbTe, carriers from the Σ band can be excited to the L band increasing the Seebeck coefficient and power factor, whereas in PbSe only the L band contributes to its p-type transport.^{23–26} This separation of valence bands accounts for the significantly lower ZT values of PbSe. Herein we show a direct route to reduce the relative energy difference between the two bands in PbSe, which allows the Σ band to contribute to the overall thermoelectric performance. Guided by our theoretical calculations we identified Cd alloying in PbSe as a powerful means of achieving better energetic convergence of the L and Σ bands that leads to an enhancement of the Seebeck coefficients and higher power factor. In addition, we simultaneously minimize band energy offsets between the PbSe matrix and nanostructured phases using compositionally alloyed $\text{CdS}_{1-x}\text{Se}_x/\text{ZnS}_{1-x}\text{Se}_x$ which allow for facile carrier transport by maintaining high hole mobility. Collectively, we show that by integrating different but synergistic concepts: (a) intramatrix band structure convergence, (b) interphase PbSe/CdS band alignment and offset minimization; and (c) with all-scale hierarchical nano/mesostructuring, we can push ZT of heavily doped p-type PbSe to reach ~ 1.6 at 923 K (Figure 1).

RESULTS AND DISCUSSION

The design strategy we describe here for improving the thermoelectric performance of PbSe involves several key steps (Figure 1), which when combined will have a maximum impact on ZT . First, we use selected second phases and Na doping to create point defects in the Pb sublattice of PbSe, reducing the thermal conductivity. Second, the nanostructured precipitates are endotaxially dispersed in the PbSe matrix, which then is mesoscale structured using spark plasma sintering to achieve small and uniform grain size to further minimize the thermal conductivity via grain boundary scattering. Third, the valence band energy levels of PbSe and those of the second phases (CdS, CdSe, ZnS and ZnSe) were calculated from density functional theory (DFT) to determine the trends in band offsets to assist in designing the optimal nanostructure phase that would reduce band offsets and minimize the adverse impact on the hole mobility. Fourth, guided by the DFT calculations, we reduce the energy difference between the light (L) and heavy (Σ) valence bands (see below) after Cd alloying, which leads to enhancements in Seebeck coefficient and power factor. Finally, to further aid in heavy valence band convergence, we use high Na doping to lower the Fermi level.

Figure 2 shows the thermoelectric properties as a function of temperature for $\text{Pb}_{0.98}\text{Na}_{0.02}\text{Se}-x\%\text{CdS}$. It is worth noting that the electrical conductivity values show negligible change with varying Cd fraction (Figure 2a), indicating CdS as a second phase does not diminish the hole mobility as seen by the trend in the measured Hall mobility values (Table S2), to be discussed later. The room temperature Seebeck coefficients are

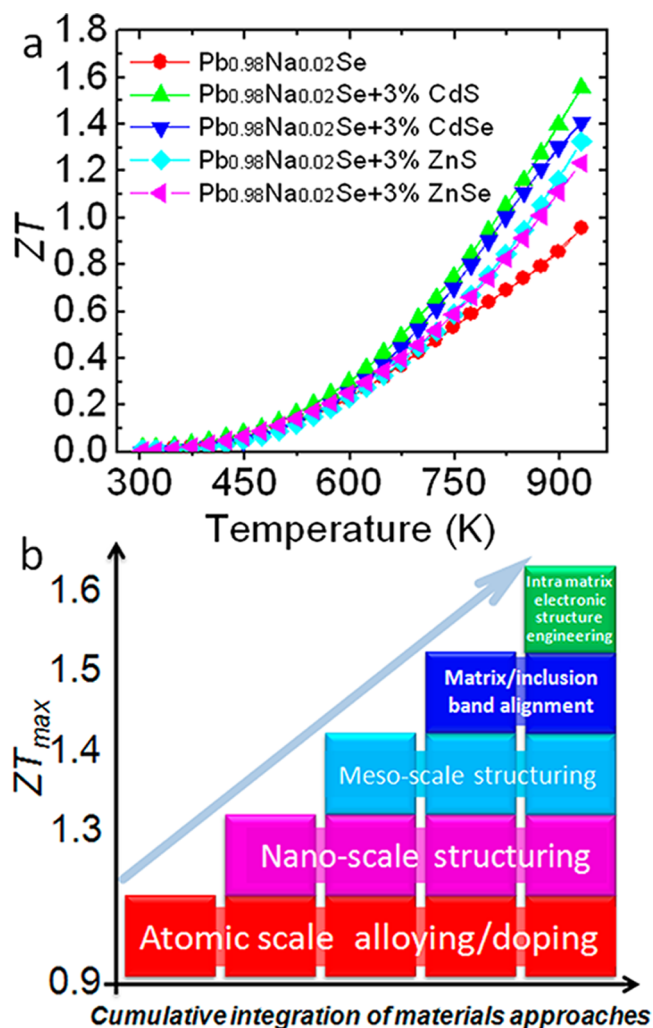


Figure 1. (a) Thermoelectric figure of merit, ZT , as a function of temperature for $\text{Pb}_{0.98}\text{Na}_{0.02}\text{Se}$ with 3.0% second phases (CdS, CdSe, ZnS, and ZnSe). (b) Cumulative integration of material approaches as a function of ZT .

positive, e.g., $\sim +21 \mu\text{V K}^{-1}$, consistent with 2.0% Na doping (Figure 2b). Upon varying the CdS fraction, the Seebeck coefficients show negligible change, suggesting the carrier concentration, which is controlled by the Na concentration, is similar for all samples. The maximum of the power factor shifts to higher temperature by the 2.0% Na doping and reaches the highest value of $\sim 14.9 \mu\text{W cm}^{-1} \text{K}^{-2}$ at 923 K. It is important to highlight that power factors for the CdS-containing samples are even higher than that of similarly doped control sample $\text{Pb}_{0.98}\text{Na}_{0.02}\text{Se}$ without second phases over the entire temperature ranges. The power factor maxima range from ~ 17.0 to $\sim 14.8 \mu\text{W cm}^{-1} \text{K}^{-2}$, as the CdS amount rises from 1.0 to 4.0% (Figure 2c). The power factors obtained here are higher than those reported previously in p-type PbSe–MSe ($M = \text{Ca}, \text{Sr}, \text{Ba}$) system.²⁷ The reasons are the improved carrier mobility and enhanced Seebeck coefficients caused by minimizing the valence band energy offsets between PbSe matrix and compositionally alloyed second phases, respectively. This will be discussed later.

The total thermal conductivity (κ_{tot}) shows a significant decrease with increasing CdS (Figure 2d), and this falling trend is also observed in κ_{lat} (Figure 2e), indicating that the dispersed CdS phase is highly effective in phonon scattering. At room

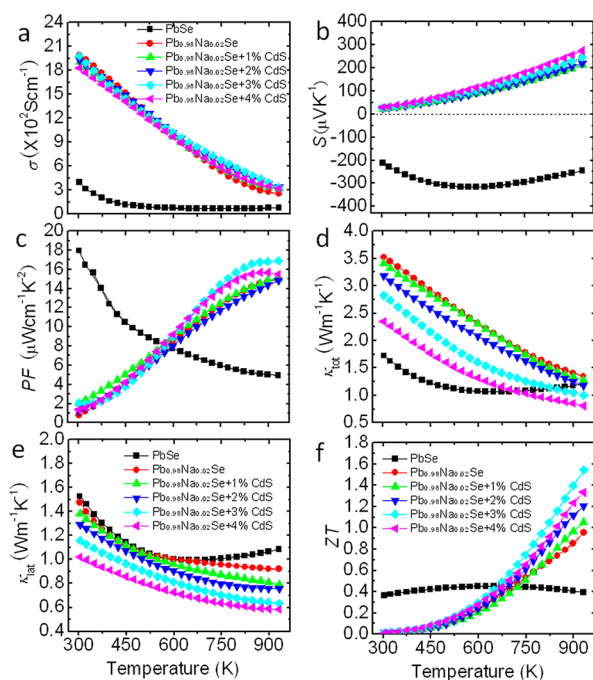


Figure 2. Thermoelectric properties as a function of temperature for $\text{Pb}_{0.98}\text{Na}_{0.02}\text{Se}-x\%\text{CdS}$: (a) Electrical conductivity; (b) Seebeck coefficient; (c) power factor; (d) total thermal conductivity; (e) lattice thermal conductivity; and (f) ZT .

temperature, the κ_{lat} decreases from $\sim 1.53 \text{ Wm}^{-1} \text{ K}^{-1}$ for pure PbSe to $\sim 1.02 \text{ Wm}^{-1} \text{ K}^{-1}$ as the CdS content is increased to 4.0%. Correspondingly, the κ_{lat} at 923 K decreases to $\sim 0.57 \text{ Wm}^{-1} \text{ K}^{-1}$ for the 4.0% CdS samples. The combined higher power factor and lower thermal conductivity of the $\text{Pb}_{0.98}\text{Na}_{0.02}\text{Se}-3.0\%\text{CdS}$ sample results in a ZT value of ~ 1.6 at 923 K (Figure 2f).

CdSe exhibits different energy levels for the conduction and valence bands compared to CdS, therefore the addition of CdSe into the PbSe matrix is expected to lead to differences in the electrical and thermal transport behaviors. Figures S4 and S5 show the thermoelectric transport behavior for the $\text{Pb}_{0.98}\text{Na}_{0.02}\text{Se}-x\%\text{CdS}$ samples. Contrary to that of CdS-containing samples, the electrical conductivity decreases with increasing amounts of CdSe over the entire temperature range, a significant difference from those of CdS, which will be discussed later. Therefore, unlike CdS the rising fraction of CdSe as a second phase significantly diminishes the hole mobility, Table S2. The ZT values for the CdSe-containing samples continue to rise up to 923 K, the maximum ZT value of ~ 1.4 at 923 K is observed for the $\text{Pb}_{0.98}\text{Na}_{0.02}\text{Se}-3.0\%\text{CdSe}$ sample. The ZnS and ZnSe were chosen for comparison to the CdS and CdSe systems as they present several substantial chemical and physical differences from CdS and CdSe. Key differences include the energy band gaps are much larger in ZnS and ZnSe and the energies of the conduction and valence band levels are different, thereby presenting larger band offsets in connection with those of PbSe. Our results confirm the theoretical predictions that Zn-containing phases are less optimal than CdS with maximum ZT values of ~ 1.3 and ~ 1.4 at 923 K achieved for $\text{Pb}_{0.98}\text{Na}_{0.02}\text{Se}-3\%\text{ZnSe}$ and $\text{Pb}_{0.98}\text{Na}_{0.02}\text{Se}-3\%\text{ZnS}$ samples, respectively (Figures S6–11).

Light Hole L/Heavy Hole Σ Bands Convergence in PbSe through Cd Alloying and Seebeck Coefficient

Enhancement. Figure 3a shows the Seebeck coefficients as a function of temperature for $\text{Pb}_{0.98}\text{Na}_{0.02}\text{Se}$ with 3.0% second

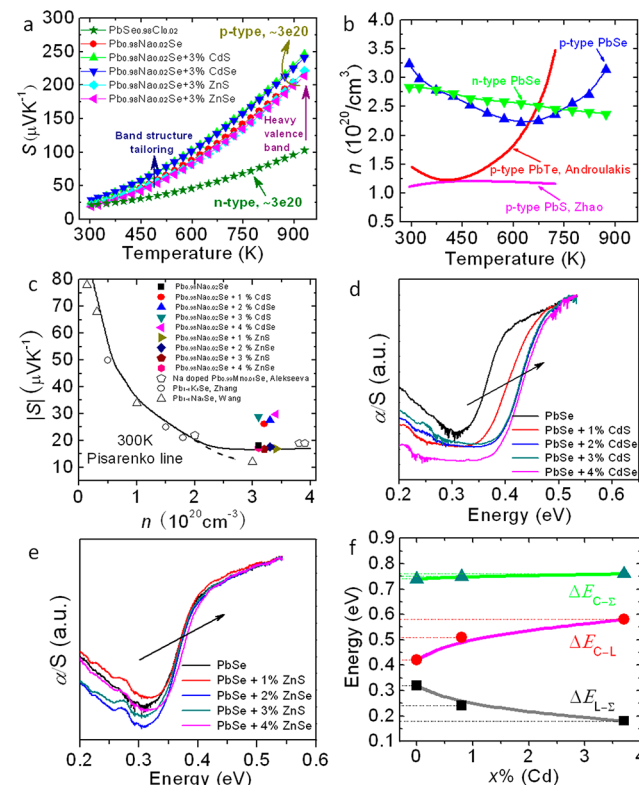


Figure 3. Seebeck coefficients and heavy valence band offsets for $\text{Pb}_{0.98}\text{Na}_{0.02}\text{Se}$ with 3.0% second phases: (a) Seebeck coefficient as a function of temperature for $\text{Pb}_{0.98}\text{Na}_{0.02}\text{Se}$ with 3.0% second phases (CdS, CdSe, ZnS, and ZnSe); n-type $\text{PbSe}_{0.98}\text{Cl}_{0.02}$ with similar carrier density is plotted for comparison; and Seebeck coefficients were enhanced by the heavy valence bands and band structure tailoring. (b) Carrier concentration as a function of temperature for PbQ (Q = Te, Se , and S^{11}). (c) Pisarenko plots at 300 K. The black solid line is the theoretical Pisarenko line that takes into account the valence band structure of PbSe,^{18,28} notice the change in curvature around $2 \times 10^{20} \text{ cm}^{-3}$. The dashed line corresponds to a single nonparabolic band with assumption of acoustic phonon scattering. Na-doped $\text{Pb}_{0.99}\text{Mn}_{0.01}\text{Se}$,¹⁸ $\text{Pb}_{1-x}\text{Na}_x\text{Se}$,²⁰ and $\text{Pb}_{1-x}\text{K}_x\text{Se}$ ²⁸ are plotted for comparison. (d) Electronic absorption spectra of PbSe samples with different CdS/CdSe fractions and without Na doping. (e) Electronic absorption spectra of PbSe samples with different ZnS/ZnSe fractions and without Na doping. (f) Band energy differences as function of Cd fractions in PbSe for the conduction (C), light hole (L), and heavy hole (Σ) bands.

phases (CdS, CdSe, ZnS, and ZnSe). The p-type PbSe samples show higher Seebeck coefficients than that of n-type controlled $\text{PbSe}_{0.98}\text{Cl}_{0.02}$ with similar carrier concentration of $\sim 3 \times 10^{20} \text{ cm}^{-3}$, especially at elevated temperature. Namely, the Seebeck coefficient at 923 K is $\sim +225\text{--}250 \mu\text{V K}^{-1}$ for p-type PbSe, whereas by comparison it is only $\sim -100 \mu\text{V K}^{-1}$ for similarly doped n-type PbSe. In addition, among the p-type samples with the same carrier concentration of $\sim 3 \times 10^{20} \text{ cm}^{-3}$, the Seebeck coefficients for the Zn-containing samples show the same levels as those of pristine $\text{Pb}_{0.98}\text{Na}_{0.02}\text{Se}$ but lower than those of the Cd-containing samples (this will be discussed later). The doubling of the Seebeck coefficients in p-type samples is related to the involvement of the heavy valence band, and it can be explained by the contribution of the Σ band at high

temperature. As the temperature increases carriers from the Σ band can be excited to the L band.²² The carrier concentration in Figure 3b shows an apparent rise with temperature in p-types PbTe and PbSe but not for n-type PbSe or p-type PbS. This thermal increase in carriers is because the interband excitations are possible between the two valence bands for PbTe and PbSe. In PbSe, the interaction of the two valence bands is apparent at about 673 K, compared to only 400 K for PbTe. Enhancements of Seebeck coefficient result from the increasing effective mass m^* by a factor of $N_v^{2/3}$. N_v is the number of degenerate valleys and is 4 for the L band and 12 for the Σ band.^{17,22} Specifically, $m^* = N_v^{2/3} m_b^*$, where m_b^* is the average (single valley) effective mass of the degenerate valleys.

Evidence for the narrowing of the L – Σ energy separation in the Cd-containing PbSe materials is shown in the Pisarenko relation between the Seebeck coefficient and carrier concentration (Figure 3c).¹² The dashed line is theoretical and corresponds to a single parabolic band assuming acoustic phonon scattering.⁹ The black solid line corresponds to a nonparabolic model that takes into account the valence band structure of PbSe.^{18,28} The Seebeck coefficients for both Na and K heavily doped PbSe fall on the black solid line.^{20,28} The flattening of the Seebeck coefficient appears at $>3 \times 10^{19} \text{ cm}^{-3}$ for PbTe²⁹ but at much higher doping levels of $>2 \times 10^{20} \text{ cm}^{-3}$ for PbSe because of its larger L – Σ energy separation.

We observed that the Cd-containing samples exhibit higher Seebeck coefficients than the Zn-containing samples in the entire temperature range of measurement, Figure 3a. This distinction between Cd and Zn may be related to their respective solubility limits in the PbSe matrix and is supported by optical spectroscopy measurements. With increasing concentrations of wide band gap CdS and CdSe, the electronic absorption spectra of PbSe samples show a widening of the band gap, Figure 3d. Since the increase of the PbSe band gap upon addition of the wide band gap metal sulfides ceases above 2% fraction, the room temperature solubility limit of Cd appears to be about 1.0–2.0%. However, in the case of ZnS/ZnSe samples, Figure 3e, no band gap changes are observed, suggesting a much lower solubility limit.

As mentioned above, the interaction of L and Σ bands with rising temperature causes an increase in the effective mass of carrier holes. Suggested by our DFT calculations, we find that Cd alloying in PbSe has a significant effect on the energies of both L and Σ bands. To investigate band energies for the conduction band (C band) and valence bands (L and Σ bands) of Cd-containing samples, we considered rock salt primitive supercell of PbSe and different concentrations of Cd addition at $\sim 1.0\%$ ($\text{Pb}_{124}\text{Cd}_1\text{Se}_{125}$) and $\sim 3.0\%$ ($\text{Pb}_{26}\text{Cd}_1\text{Se}_{27}$) to investigate band changes. Calculations for the Zn case were not carried out since no solid solubility of Zn in PbSe was observed. The calculated band structures for PbSe, $\text{Pb}_{0.99}\text{Cd}_{0.01}\text{Se}$, and $\text{Pb}_{0.97}\text{Cd}_{0.03}\text{Se}$ are given in Figure S12. As shown in Figure 3f, increasing Cd concentration increases band gap, i.e., in the energy separation between L and C bands (ΔE_{C-L}) which is consistent with the experimental band gap measurements (Figure 3d). While the energy of the Σ band remains roughly constant with respect to the C band, showing negligible changes of $\Delta E_{C-\Sigma}$ with Cd alloying, the two valence bands (L and Σ) move closer in energy ($\Delta E_{L-\Sigma}$). With rising temperature, further convergence of L and Σ bands could occur through band broadening. The contribution of Σ band at high temperatures increases the effective mass (Table S2) and enhances the Seebeck coefficient. In other words, the energy

separation between the L and Σ bands decreases with Cd alloying. Therefore, the alloying of Cd on the cation sublattice of PbSe makes $\text{Pb}_{1-x}\text{Cd}_x\text{Se}$ more similar to PbTe in terms of the heavy valence band convergence. The predictions of band convergence from DFT are confirmed by the measured enhancement of the Seebeck coefficient, shown in Figure 3a,c. The Seebeck coefficient enhancement is similar in character to that caused by resonant states.^{13,30} Namely, the Cd-containing samples show enhancements of 10 and 25 $\mu\text{V K}^{-1}$ in Seebeck coefficient at 300 and 923 K, respectively. This Seebeck enhancement via intramatrix electronic structure engineering is a key enabling strategy to achieve the high ZT obtained in this work.

Valence Band Energy Offsets Between PbSe Matrix and MQ Second Phases and Electrical Conductivity.

In order to further illustrate the effects of these metal sulfide and selenide nanostructures on the thermoelectric properties of p-type PbSe, we make a comparison as a function of all relevant second phases, e.g., CdS, CdSe, ZnS, and ZnSe. Figure S13a shows the temperature-dependent electrical conductivities for $\text{Pb}_{0.98}\text{Na}_{0.02}\text{Se}$ with 3.0% second phases (CdS, CdSe, ZnS, and ZnSe), since 3.0% is the optimized fraction for all systems resulting in the best thermoelectric performance. It is readily seen that the electrical conductivities for the CdS/ZnS-containing samples outperform those of CdSe/ZnSe-containing samples over the entire measurement temperature range. Also, it can be clearly seen that CdS/ZnS-containing samples retain nearly the same levels of electrical conductivity as the control sample of $\text{Pb}_{0.98}\text{Na}_{0.02}\text{Se}$. Since the carrier concentration is similar for all samples and controlled by fixing the 2.0% Na doping, the variations of electrical conductivity are attributed to the carrier mobility. Interestingly, with an increase in the second-phase fraction, the carrier mobilities for the CdS/ZnS samples show negligible changes. In contrast, a decreasing trend is observed for the CdSe/ZnSe-containing samples (Figure 4a).

We will now discuss how the hole carrier mobility is affected by the valence band offsets between the host PbSe matrix and the nanostructured second-phase precipitates. DFT calculations of band alignment show (Figure 4b) that, relative to PbSe, the valence band energy differences are 0.06, 0.27, 0.13, and 0.30 eV for CdSe, CdS, ZnSe and ZnS, respectively. Details of the DFT calculations for these energy barriers can be found in Figure S14. The reduced electron mobility for CdSe/ZnSe samples indicates relatively strong scattering of holes across the (CdSe/ZnSe)/PbSe interfaces, whose energy offsets are relatively large.³¹ Clearly the band offsets between perfectly ordered, stoichiometric phases are not sufficient to explain the observed behavior. However, EDX analysis on these nanoprecipitates (Figures S15 and S16) suggests that when CdS/ZnS are introduced in the PbSe matrix, the nanoprecipitates are not perfectly stoichiometric but rather form solid solutions of the type $\text{CdS}_{1-x}\text{Se}_x/\text{ZnS}_{1-x}\text{Se}_x$ (Figure 4b). We assert that the valence band energy levels for $\text{CdS}_{1-x}\text{Se}_x/\text{ZnS}_{1-x}\text{Se}_x$ will be intermediate between the valence band energies of CdS/ZnS and CdSe/ZnSe (though not necessarily linear in x ; Figure 4b is only a schematic illustration) and achieve excellent energy level alignments (minimal offset) with the PbSe matrix. To verify this assumption, we selectively calculated the valence band alignment of $\text{CdS}_{0.9}\text{Se}_{0.1}$. As expected, the valence band energy level for $\text{CdS}_{0.9}\text{Se}_{0.1}$ lies between those of CdS and CdSe. This type of band-offset engineering that takes advantage of the electronic bands of the nonstoichiometric nanostructures

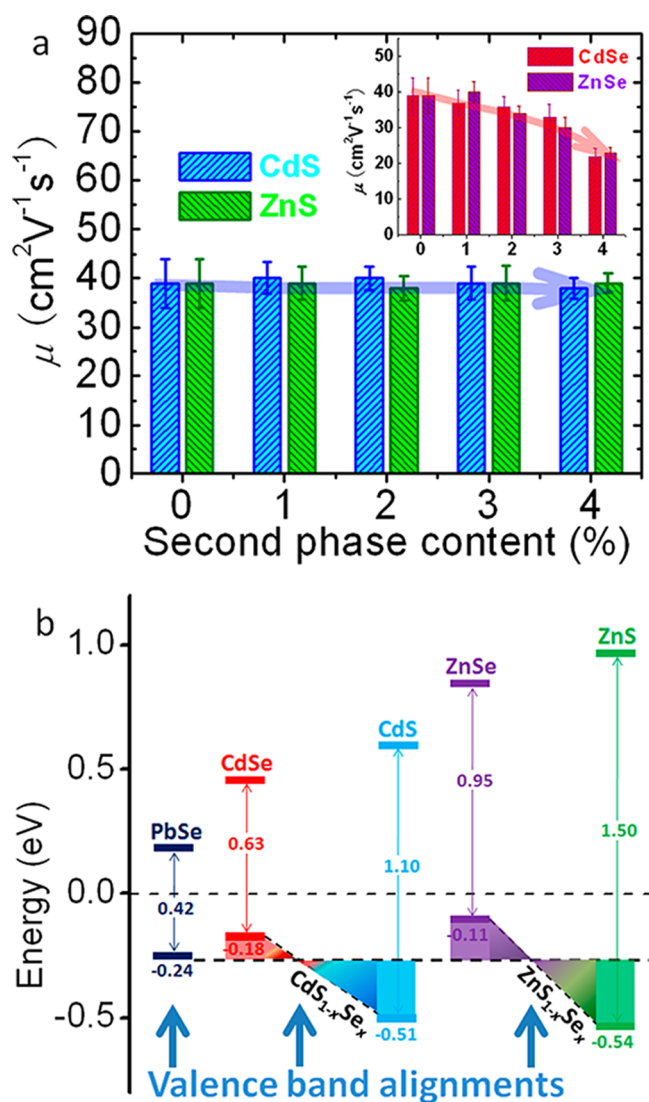


Figure 4. Carrier mobility and valence band alignments for $\text{Pb}_{0.98}\text{Na}_{0.02}\text{Se}$ with 3.0% second phases: (a) Carrier mobility as a function of second-phase contents for $\text{Pb}_{0.98}\text{Na}_{0.02}\text{Se}$ with $x\%$ CdS (ZnS) with similar carrier concentration of $\sim 3 \times 10^{20} \text{ cm}^{-3}$, inset shows $x\%$ CdSe (ZnSe)-containing samples, the carrier mobilities for the CdS/ZnS-containing samples show negligible changes. (b) DFT band alignments of the conduction band (CB) and valence band (VB) energy levels for PbSe, CdS, CdSe, ZnS, and ZnSe. $\text{CdS}_{1-x}\text{Se}_x$ and $\text{ZnS}_{1-x}\text{Se}_x$ solid solutions show a energy levels bridging. All calculations are in the NaCl structure, and CdS and ZnS are from ref 16.

is a new insight and allows facile carrier transport between matrix and nanostructure.^{15,16}

All-Scale Hierarchical Structuring: Reduction of Lattice Thermal Conductivity via nano/meso-structuring. The total thermal conductivities for the samples having CdS, CdSe, ZnS, and ZnSe additions are at comparable levels and show the same trend as a function of temperature (Figure S13c). The lattice thermal conductivity is strongly reduced by introducing second phases (Figure S13d), underscoring the high efficacy of the binary sulfide and selenide nanostructures in strong scattering of phonons. Specifically, at room temperature, the lattice thermal conductivity decreases from $\sim 1.53 \text{ W m}^{-1} \text{ K}^{-1}$ for pure PbSe to ~ 1.16 , ~ 1.18 , ~ 1.20 , and $\sim 1.18 \text{ W m}^{-1} \text{ K}^{-1}$ for the CdS-, CdSe-, ZnS-, and ZnSe-containing samples,

respectively. Correspondingly, the lattice thermal conductivity at 923 K decreases to ~ 0.63 , ~ 0.64 , ~ 0.72 , and $\sim 0.73 \text{ W m}^{-1} \text{ K}^{-1}$ for CdS, CdSe, ZnS, and ZnSe samples, respectively.

The presence of nanostructures and mesoscale grains in the PbSe matrix is confirmed by our TEM studies. The low-magnification TEM image (Figure 5a) highlights the grain size

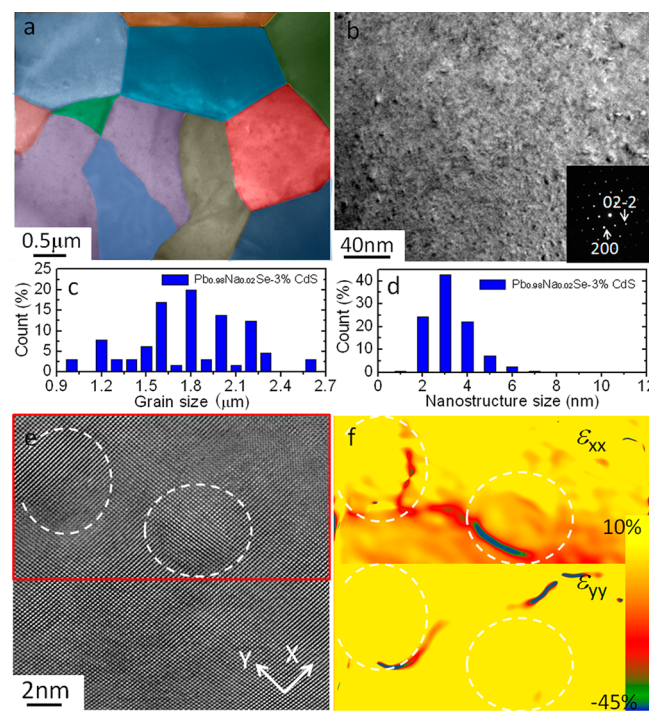


Figure 5. Micro and nanostructures for $\text{Pb}_{0.98}\text{Na}_{0.02}\text{Se}-3.0\%\text{CdS}$: (a) Low-magnification TEM image showing mesoscale grains. (b) Medium-magnification TEM images showing nanostructures. (c) Grain size distribution histogram of (a). (d) Precipitate size distribution of (c). (e) The crystallography alignment between the precipitates and the matrix. The corresponding strain maps along ϵ_{xx} (f, top) and ϵ_{yy} (f, bottom) are also shown which is highlighted by red line in (e).

for the $\text{Pb}_{0.98}\text{Na}_{0.02}\text{Se}-3\%\text{CdS}$ polycrystalline sample as being $\sim 1-2 \mu\text{m}$ (Figure 5c). From the medium-magnification images shown in Figure 5b, small precipitates with size from 2 to 10 nm are observed for $\text{Pb}_{0.98}\text{Na}_{0.02}\text{Se}-3\%\text{CdS}$, and the size distribution of the precipitates is depicted in the histogram of Figure 5d. The inset of Figure 5b is the respective electron diffraction pattern, taken from a selected area aperture to include the matrix and several precipitates. The absence of extra Bragg spots is consistent with the endotaxial crystallographic alignment between the matrix and the precipitates.^{11,16} The number density for precipitates is estimated to be about $9.12 \times 10^{18} \text{ cm}^{-3}$ for $\text{Pb}_{0.98}\text{Na}_{0.02}\text{Se}-3\%\text{CdS}$ and $8.12 \times 10^{18} \text{ cm}^{-3}$ for $\text{Pb}_{0.98}\text{Na}_{0.02}\text{Se}-3\%\text{ZnSe}$ (Figure S17). The high-resolution phase contrast image (Figure 5e) further confirms the crystallographic endotaxial alignment. Spatially distributed semiquantitative strain analysis was performed by the geometric phase analysis³² technique to determine the presence of relative elastic/plastic strain in reference to the matrix. The strain maps along ϵ_{xx} and ϵ_{yy} of $\text{Pb}_{0.98}\text{Na}_{0.02}\text{Se}-3\%\text{CdS}$ are shown in Figure 5f. The maps illustrate elastic strain at the boundaries circled by the dotted line. Furthermore, the circle line profile in Figure 5f depicts the lattice mismatch of the precipitate and the matrix of about 8% (Figure S18). High-resolution images of correspond-

ing strain maps and the lattice mismatch for the $\text{Pb}_{0.98}\text{Na}_{0.02}\text{Se}-3\%\text{ZnSe}$ sample can be found in Figure S19. The observed nanostructured precipitates and strains are believed to have an exceptional influence on the broad-based phonon scattering on multiple length scales.

CONCLUDING REMARKS

The integration of band structure engineering (both intraphase $L-\Sigma$ band convergence and interphase band offset gap tailoring) with all-scale hierarchical structuring pushes ZT to the highest level for p-type PbSe (with CdS nanostructures) of ~ 1.6 at 923 K. This ZT value is a record for a Te-free thermoelectric material and approaches the theoretically predicted value of 1.8. Cd alloying reduces the energy separation of the two valence bands L and Σ by lowering the energy of the former, which creates an enhancement of the Seebeck coefficient, by as high as $\sim 25 \mu\text{V K}^{-1}$ at 923 K. At the same time the valence band alignment between the PbSe matrix and $\text{CdS}_{1-x}\text{Se}_x$ nanostructures facilitates carrier transport without appreciable energy barriers across the samples, while all-scale hierarchical structuring strongly reduces the lattice thermal conductivity to very low values near $\sim 0.63 \text{ W m}^{-1} \text{ K}^{-1}$. Given that these values are still higher than the “minimal lattice thermal conductivity” value of $\sim 0.36 \text{ W m}^{-1} \text{ K}^{-1}$, as calculated for Pb–Te–Se by the approach of Cahill,³³ it seems to leave room for even higher ZT values in this system. We call the integration of multiple concepts a *panoscopic* approach that could be applicable to other systems with crystal and electronic band structures amenable to similar tailoring and nanostructuring.

ASSOCIATED CONTENT

Supporting Information

Experimental details. Density of samples included in the study (Table S1); Transport properties of PbSe with CdS/CdSe and ZnS/ZnSe (Table S2); Powder XRD patterns of $\text{Pb}_{0.98}\text{Na}_{0.02}\text{Se}$ with x at. % CdS (Figure S1); Thermoelectric properties as a function of temperature for $\text{Pb}_{0.98}\text{Na}_{0.02}\text{Se}$ with x at. % CdS (Figure S2); Powder XRD patterns of $\text{Pb}_{0.98}\text{Na}_{0.02}\text{Se}$ with x at. % CdSe (Figure S3); Thermoelectric properties as a function of temperature for $\text{Pb}_{0.98}\text{Na}_{0.02}\text{Se}$ with x at. % CdSe (Figures S4 and S5); Powder XRD patterns of $\text{Pb}_{0.98}\text{Na}_{0.02}\text{Se}$ with x at. % ZnSe (Figure S6); Thermoelectric properties as a function of temperature for $\text{Pb}_{0.98}\text{Na}_{0.02}\text{Se}$ with x at. % ZnSe (Figures S7 and S8); Powder XRD patterns of $\text{Pb}_{0.98}\text{Na}_{0.02}\text{Se}$ with x at. % ZnS (Figure S9); Thermoelectric properties as a function of temperature for $\text{Pb}_{0.98}\text{Na}_{0.02}\text{Se}$ with x at. % ZnS (Figures S10 and S11); Band structures for PbSe, $\text{Pb}_{0.99}\text{Cd}_{0.01}\text{Se}$ and $\text{Pb}_{0.97}\text{Cd}_{0.03}\text{Se}$ (Figure S12); Thermoelectric properties as a function of temperature for $\text{Pb}_{0.98}\text{Na}_{0.02}\text{Se}$ with 3.0% second phases (CdS, CdSe, ZnS and ZnSe) (Figure S13); Band gap alignment of the metal sulfides, PbSe, CdSe, $\text{CdS}_{0.9}\text{Se}_{0.1}$ and CdS (Figure S14); STEM image of $\text{Pb}_{0.98}\text{Na}_{0.02}\text{Se}-3.0\%\text{CdS}$ sample (Figure S15); STEM and the quantitative analysis of $\text{Pb}_{0.98}\text{Na}_{0.02}\text{Se}-3\%\text{ZnS}$ (Figure S16); Medium-magnification TEM images and the distribution of precipitates with different sizes for $\text{Pb}_{0.98}\text{Na}_{0.02}\text{Se}-3.0\%\text{ZnSe}$ (Figure S17); Lattice mismatch analysis for $\text{Pb}_{0.98}\text{Na}_{0.02}\text{Se}-3.0\%\text{CdS}$ (Figure S18); High-resolution image and strain maps of $\text{Pb}_{0.98}\text{Na}_{0.02}\text{Se}-3\%\text{ZnSe}$ (Figure S19). This material is available free of charge via the Internet at <http://pubs.acs.org>.

AUTHOR INFORMATION

Corresponding Author

m-kanatzidis@northwestern.edu

Author Contributions

[†]These authors contributed equally.

Notes

The authors declare no competing financial interest.

ACKNOWLEDGMENTS

This work was also supported in part by a grant DOE-EERE/NSF (CBET-1048728) (L.-D.Z. and M.G.K.). The transmission electron microscopy, spark plasma sintering, and density functional calculations in this work were supported as part of the Revolutionary Materials for Solid State Energy Conversion, an Energy Frontier Research Center funded by the U.S. Department of Energy, Office of Science, and Office of Basic Energy Sciences under award no. DE-SC0001054 (S.-H.L., S.H., C.-I.W., X.Z., C.U., C.W., T.P.H., and V.P.D.). Transmission electron microscopy work was performed in the (EPIC) (NIFTI) (Keck-II) facility of NUANCE Center at Northwestern University. The NUANCE Center is supported by NSF-NSEC, NSF-MRSEC, Keck Foundation, the State of Illinois, and Northwestern University. We acknowledge use of the Office of Naval Research DURIP-supported Pulsed Electric Current Sintering System at Michigan State University.

REFERENCES

- (1) (a) Kanatzidis, M. G. *Chem. Mater.* **2010**, *22*, 648. (b) Kanatzidis, M. G. *Semicond. Semimetals* **2000**, *69*, 51.
- (2) (a) Sootsman, J. R.; Chung, D. -Y.; Kanatzidis, M. G. *Angew. Chem., Int. Ed.* **2009**, *48*, 8616. (b) Vineis, C. J.; Shakouri, A.; Majumdar, A.; Kanatzidis, M. G. *Adv. Mater.* **2010**, *22*, 3970.
- (3) (a) Zebarjadi, M.; Esfarjani, K.; Dresselhaus, M. S.; Ren, Z. F.; Chen, G. *Energy Environ. Sci.* **2012**, *5*, 5147. (b) Liu, W. S.; Yan, X.; Chen, G.; Ren, Z. F. *Nano Energy* **2012**, *1*, 42.
- (4) (a) Snyder, J. G.; Toberer, E. S. *Nat. Mater.* **2008**, *7*, 105. (b) Li, J. F.; Liu, W. S.; Zhao, L. D.; Zhou, M. *NPG Asia Mater.* **2010**, *2*, 152.
- (5) Chen, G.; Dresselhaus, M. S.; Dresselhaus, G.; Fleurial, J. -P.; Caillat, T. *Int. Mater. Rev.* **2003**, *48*, 45.
- (6) Hsu, K. F.; Loo, S.; Guo, F.; Chen, W.; Dyck, J. S.; Uher, C.; Hogan, T.; Polychroniadis, E. K.; Kanatzidis, M. G. *Science* **2004**, *303*, 818.
- (7) Biswas, K.; He, J.; Blum, I. D.; Wu, C.; Hogan, T.; Seidman, D. N.; D'David, V. P.; Kanatzidis, M. G. *Nature* **2012**, *489*, 414.
- (8) Poudel, B.; Hao, Q.; Ma, Y.; Lan, Y.; Minnich, A.; Yu, B.; Yan, X.; Wang, D.; Muto, A.; Vashaee, D.; Chen, X.; Liu, J.; Dresselhaus, M. S.; Chen, G.; Ren, Z. F. *Science* **2008**, *320*, 634.
- (9) Androulakis, J.; Todorov, I.; He, J. Q.; Chung, D. -Y.; Dravid, V. P.; Kanatzidis, M. G. *J. Am. Chem. Soc.* **2011**, *133*, 10920.
- (10) Zhao, L.-D.; Lo, S.-H.; He, J. Q.; Li, H.; Biswas, K.; Androulakis, J.; Wu, C.-I.; Hogan, T. P.; Chung, D.-Y.; Dravid, V. P.; Kanatzidis, M. G. *J. Am. Chem. Soc.* **2011**, *133*, 20476.
- (11) Zhao, L.-D.; He, J. Q.; Wu, C.-I.; Hogan, T. P.; Zhou, X. Y.; Uher, C.; Dravid, V. P.; Kanatzidis, M. G. *J. Am. Chem. Soc.* **2012**, *134*, 7902.
- (12) Heremans, J. P.; Jovovic, V.; Toberer, E. S.; Saramat, A.; Kurosaki, K.; Charoenphakdee, A.; Yamanaka, S.; Snyder, G. J. *Science* **2008**, *321*, 554.
- (13) Harman, T. C.; Taylor, P. J.; Walsh, M. P.; LaForge, B. E. *Science* **2002**, *297*, 2229.
- (14) Heremans, J. P.; Thrush, C. M.; Morelli, D. T. *Phys. Rev. B* **2004**, *70*, 115334.
- (15) Biswas, K.; He, J. Q.; Zhang, Q. C.; Wang, G. Y.; Uher, C.; Dravid, V. P.; Kanatzidis, M. G. *Nat. Chem.* **2011**, *3*, 160.

- (16) Zhao, L. D.; He, J. Q.; Hao, S. Q.; Wu, C. I.; Hogan, T. P.; Wolverton, C.; Dravid, V. P.; Kanatzidis, M. G. *J. Am. Chem. Soc.* **2012**, *134*, 16327.
- (17) Pei, Y. Z.; Shi, X.; LaLonde, A.; Wang, H.; Chen, L.; Snyder, G. *J. Nature* **2011**, *473*, 66.
- (18) Alekseeva, G. T.; Gurieva, E. A.; Konstantinov, P. P.; Prokofeva, L. V.; Ravich, Y. I. *Semiconductors* **1997**, *31*, 446.
- (19) Wang, H.; Pei, Y. Z.; LaLonde, A. D.; Snyder, G. J. *Proc. Natl. Acad. Sci. U.S.A.* **2012**, *109*, 9705.
- (20) Wang, H.; Pei, Y. Z.; LaLonde, A. D.; Snyder, G. J. *Adv. Mater.* **2011**, *23*, 1366.
- (21) Parker, D.; Singh, D. J. *Phys. Rev. B* **2010**, *82*, 035204.
- (22) Ravich, I. I.; Efimova, B. A.; Smirnov, I. A. *Semiconducting lead chalcogenides*; Plenum Press: New York, 1970.
- (23) Rogers, L. M.; Crocker, A. J. *J. Phys. D: Appl. Phys.* **1971**, *4*, 1006.
- (24) Rogers, L. M.; Crocker, A. J. *J. Phys. D: Appl. Phys.* **1971**, *5*, 1671.
- (25) Bhandari, C. M.; Rowe, D. M. In *CRC Handbook of Thermoelectrics*; Rowe, D. M., Ed.; CRC Press, Boca Raton, FL, 1995, p 45.
- (26) Smirnov, I. A.; Vinograd, M.; Kolomoet, N.; Sysoeva, L. M. *Sov. Phys. Solid State USSR* **1968**, *9*, 2074.
- (27) Lee, Y.; Lo, S. H.; Androulakis, J.; Wu, C. I.; Zhao, L. D.; Chung, D. Y.; Hogan, T.; Dravid, V.; Kanatzidis, M. G. *J. Am. Chem. Soc.* **2013**, *135*, 5152.
- (28) Zhang, Q.; Cao, F.; Lukas, K.; Liu, W. S.; Esfarjani, K.; Opeil, C.; Broido, D.; Parker, D. S.; Singh, D. J.; Chen, G.; Ren, Z. F. *J. Am. Chem. Soc.* **2012**, *134*, 10031.
- (29) Pei, Y. Z.; Heinz, N. A.; LaLonde, A.; Snyder, G. J. *Energy Environ. Sci.* **2011**, *4*, 3640.
- (30) Heremans, J. P.; Wiendlocha, B.; Chamoire, A. M. *Energy Environ. Sci.* **2012**, *5*, 5510.
- (31) Fang, F.; Opila, R. L.; Venkatasubramanian, R.; Colpitts, T. J. *Vac. Sci. Technol., A* **2011**, *29*, 031403.
- (32) Hÿtch, M. J.; Snoeck, E.; Kilaas, R. *Ultramicroscopy* **1998**, *74*, 131.
- (33) Koh, Y. K.; Vineis, C. J.; Calawa, S. D.; Walsh, M. P.; Cahill, D. G. *Appl. Phys. Lett.* **2009**, *94*, 153101.